TURBO-22-1279

LES-CHT for a Rotating Cavity With Axial Throughflow

Tom Hickling [*], **Li He**
Department of Engineering Science
University of Oxford
Oxford, OX1 3PJ, UK
Email: tom.hickling@eng.ox.ac.uk

ABSTRACT

The flow and heat transfer within rotating cavities is often discussed as a conjugate problem: the temperature distribution within the cavity disks drives the large-scale flow structure within the cavity, and the cavity aerodynamics influence the heat transfer to the disks. However, most simulations of rotating cavities only consider the fluid domain in isolation. This is particularly true for turbulence resolving approaches such as large eddy simulation (LES).

The large timescale disparity between the fluid time steps used in LES and the characteristic solid time-scale complicates the use of LES with conjugate heat transfer (CHT). A further issue is that an under-resolved solid mesh artificially amplifies higher frequency temperature fluctuations from the fluid.

This paper addresses these challenges with a new method for LES-CHT where the low-frequency temperature fluctuation caused by the large-scale flow structure is accounted for using a multi-scale frequency domain approach. We investigate two cases: axially heated disks made of a low conductivity material, and disks made from a higher conductivity material with a temperature set by radial conduction from the shroud.

The formation of small-scale flow structures on both the disk and shroud is dependent on the heating configuration of the cavity - indicating that high-fidelity thermal boundary conditions

[*]Address all correspondence to this author.

should be used when simulating rotating cavities. The formation of heating induced vortical flow structures near the disk is particularly interesting, as this is unexpected from the laminar Ekman layer modelling argument usually used to consider this region.

1 Introduction

1.1 Rotating Cavity Background

As gas turbine cores reduce in size, the size of the high pressure compressor blade tip clearance relative to the height of the main gas path increases. Keeping this clearance small at cruise conditions while avoiding the blade tip rubbing on the compressor casing at high-power conditions is important for designing an efficient engine. As one of the main factors governing the tip-clearance is the thermal expansion of the disks that bound the rotating cavities inside the compressor (Fig. 1), there is a need to better understand and model the flow and heat transfer within them.

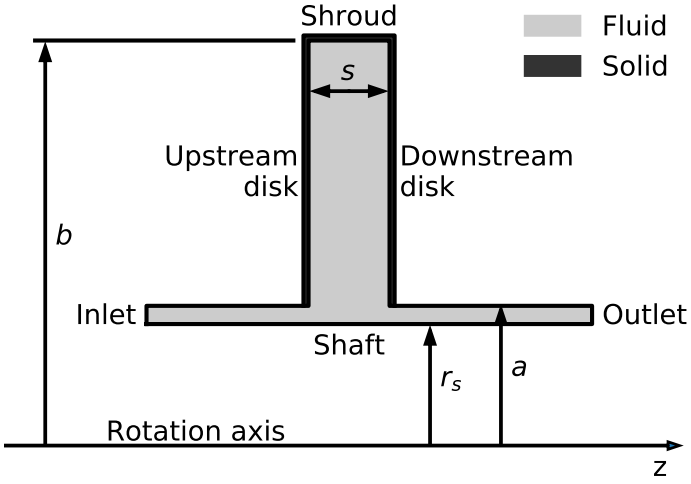

Fig. 1. Cavity dimensions (to scale) and nomenclature.

The shroud of the rotating cavity is usually hotter than the axial throughflow at the bottom of the disks. This sets up an unstable density gradient in which the centrifugal and Coriolis forces interact to form a well known global flow structure that slips relative to the cavity. The large-scale flow structure consists of pairs of cyclonic and anti-cyclonic circulations with regions of radial outflow and inflow between them that transport cold fluid from the axial throughflow to the shroud and back again. The

cyclonic circulation has a region of lower pressure at its centre, and the anti-cyclonic circulation has a region of higher pressure.

Three dimensionless groups can be used to fully define a bulk description of rotating cavity flows: the axial Reynolds number Re_z, the rotational Reynolds number Re_ϕ, and the buoyancy parameter $\beta\Delta T_{max}$. These are given by

$$Re_z = \frac{\rho V_{z,in} b}{\mu_{in}}, \tag{1}$$

$$Re_\phi = \frac{\rho \Omega b^2}{\mu_{in}}, \tag{2}$$

$$\beta\Delta T_{max} = \frac{T_{max}}{T_{in}} - 1, \tag{3}$$

where ρ is density, $V_{z,in}$ is the inlet axial velocity, μ_{in} is the cavity inlet dynamic viscosity, Ω is the cavity angular velocity, and T_{max} and T_{in} are the maximum wall temperature and the static temperature of the inlet axial throughflow respectively.

It is becoming widely accepted that LES is the most appropriate turbulence modelling fidelity for the flow within rotating cavities. Hickling and He [1] showed that although unsteady Reynolds averaged Navier-Stokes (URANS) can give sensible area-averaged results in some cases, this is due to a fortunate cancellation of errors, and that the model does not predict the correct details of the flow structure and is not suitable for use in rotating cavities. This paper also showed that it is not suitable to use wall modelling approaches such as detached eddy simulation (DES) in these flows. This was because the radial inflow transports URANS eddy viscosity generated near the shroud into the bulk cavity flow where it is non-physical and causes an incorrect enhancement of the disk heat transfer. On the shroud, it was found that the extra eddy viscosity suppressed heat-transfer enhancing streaks, and did not adequately

model their effects.

Both the near-disk and the near-shroud flow is very sensitive to thermal effects: on the shroud, buoyancy generated flow structures that enhance the local heat transfer have been observed by several authors [1–4] On the disks, Gao et al. [5, 6] found that the inclusion of viscous heating can affect heat transfer predictions due to the laminar nature of the disk Ekman layers. Similarly, Hickling and He [1] showed that the average disk shear stress was different when comparing an adiabatic and an isothermal disk with the same overall temperature difference.

The sensitivity of the flow structures within the rotating cavity to local heat transfer effects suggests that it is necessary to model the flow within rotating cavities with conjugate heat transfer (CHT) to properly capture the interaction of the cavity heating and aerodynamics. Most papers that investigate this use a steady RANS fluid domain solution [7, 8] which - although more simple to properly couple to a solid domain solution - is not able to accurately capture the fluid domain physics. To the best of the author's knowledge, the only paper that has considered unsteady CHT of a rotating cavity is by Tian et al. [9], who used URANS and observed a significant reduction in the downstream disk Nusselt number when comparing CHT to stand-alone fluid domain results.

1.2 LES-CHT Background

From the above discussion, our motive for carrying out LES-CHT computations on rotating cavities is clear. However, this is not straightforward due to two important multi-scale challenges: the large time-scale disparity between the solid and fluid domain time-scales; and the wall-normal mesh spacing that is required to resolve the thermal penetration depth of high frequency wall temperature fluctuations.

The time-scale disparity usually manifests itself when calculating through the initial transient - in general the characteristic time-scale for the solid domain is four orders of magnitude greater than any characteristic time-scales in the fluid domain. This is particularly an issue for LES, where very small time-steps are often required in the fluid domain to maintain Courant-Friedrichs-Lewy (CFL) numbers below unity. A common approach for managing this issue is the approach taken in the unsteady CHT computations by He and Oldfield [10] and He [11]: couple a moving average of the wall-adjacent temperature in the fluid domain to a steady-state solid domain, bypassing the challenge of the solid domain initial transient.

If a 1D semi-infinite solid domain with thermal diffusivity α is subject to a sinusoidal wall temperature fluctuation at frequency f, the magnitude of the temperature fluctuations within the solid domain will decrease in proportion to $\exp(-x\sqrt{\pi f/\alpha})$, where x is the distance from the wall where the temperature fluctuation is applied [12]. This leads to the concept of a thermal penetration depth, which we take to be the value of x where the temperature fluctuation amplitude has reduced to 1% of its wall value. The thermal penetration depth can be calculated as

$$\delta_P = \frac{\ln(100)}{\sqrt{\pi}}\sqrt{\alpha/f}. \tag{4}$$

Fadl and He [13] investigated the effect of under-resolving the thermal penetration depth in the solid domain (i.e. having a wall-normal mesh spacing larger than δ_P). By assuming a linear variation of wall temperature within the thermal penetration depth, they were able to show that for a given fluctuating wall heat flux, the wall temperature fluctuations would be erroneously amplified, and that this amplification would grow linearly with $\sqrt{f}$ as δ_P reduced. Depending on the mesh spacing and material properties, this artificial amplification could reach over an order of magnitude. This has been observed in LES of natural convection by Fadl and He [13] and in combustors by Shahi et al. [14].

He and Oldfield [10] and He [11] used a wall transfer function approach to directly relate the temperature fluctuations at the wall-adjacent fluid cell centre to the temperature fluctuation on the wall. They derived the transfer function by considering the analytical solution for the unsteady wall heat-flux response of a 1D semi-infinite solid domain subject to an imposed unsteady wall-temperature. The harmonic heat-flux is evaluated using a single-sided finite difference in the fluid domain to give an expression for the complex Fourier harmonic of the wall temperature fluctuation $\widehat{T'_w}$ in terms of the cell centre temperature fluctuation harmonic $\widehat{T'_f}$ as

$$\widehat{T'_w} = \widehat{C_w}\widehat{T'_f}, \tag{5}$$

where the wall transfer function $\widehat{C_w}$ is given at angular frequency ω by

$$\widehat{C_w} = \frac{\widetilde{h_f}}{\widetilde{h_f} + \sqrt{\widetilde{\rho}_s \widetilde{c}_s \widetilde{k}_s} \sqrt{i\omega}}. \tag{6}$$

Here, ρ_s, c_s, and k_s are the solid domain density, specific heat capacity, and thermal conductivity, and h_f is the fluid side heat transfer coefficient, given by $k_f/\Delta x_f$, where Δx_f is the normal distance from the fluid cell centre to the coupled wall. LES studies have been previously conducted using this approach - in [11] a significant reduction in the amplitude of the wall temperature fluctuation was found, and in [15] it was found to increase the magnitude of the wall heat flux fluctuation.

This challenge in rotating cavities is that the slip of the large-scale flow structure causes a very low frequency temperature fluctuation near the disks [1], which may have a penetration depth that is similar to (or even greater than) the solid domain thickness. This means that it is desirable to develop an approach that allows us to capture frequencies of unsteadiness in the solid domain when the thermal penetration depth is of a similar magnitude to the solid domain thickness so that any non-local interactions can be captured, but also allows us to use the wall transfer function approach for fluctuations that we do not need to solve/are not able to resolve properly in the solid domain.

1.3 Overview of the Paper

In this paper, the key question that we would like to address is: *does the flow structure within the cavity depend on the exact details of the local heating?* If there is a significant dependence (in terms of either the large-scale aerodynamics or smaller scale local flow features) then it is a good indication that CHT should be used when simulating these flows.

After validating our LES simulations on a fluid domain only baseline case, we present a new multi-scale method for LES-CHT that extends previous work with the 1D semi-infinite wall transfer function by He [11] to be able to calculate low frequency/high penetration depth thermal unsteadiness directly in the solid domain by using a time-spectral solution method. We use this method to investigate two CHT cases: the first has axially heated disks and an adiabatic external boundary conditions on the shroud, and the second radially heated case has a fixed hot shroud temperature and adiabatic external boundary

conditions on the disks. The flow fields from these cases are then compared with the above question in mind.

2 Baseline LES Simulations

2.1 Case Information

To validate our fluid domain LES, we carried out computations on the experimental test rig of Bohn et al. [16]. In this experiment, 5 mm thick epoxy disks were heated to provide a radially increasing temperature distribution, and the disk heat fluxes and wall temperatures were measured.

A diagram of our fluid and solid domains is shown in Fig.1, and the values of the cavity dimensions and other key parameters is given in Tab. 1. The cavity dimensions and fluid domain geometry are chosen to match those of the experimental rig of Bohn et al. [16], and the solid domain geometry is broadly representative of the rig (although not identical). Note we use a different definition of the axial Reynolds number to [16], this is to be consistent with more recent publications on rotating cavities. Key features to note are the upstream and downstream disks at $z/s = -0.5$ and $z/s = 0.5$ respectively, and the axial mid-plane at $z/s = 0$. The values of the dimensionless parameters in Tab. 1 give a Grashof number of

$$Gr = \left(1 - \frac{a}{b}\right)^3 {Re_\phi}^2 \beta \Delta T_{\max} = 4.86 \times 10^{10} \tag{7}$$

and a theoretical laminar Ekman layer thickness of

$$\delta_{\mathrm{Ek}} = \frac{\pi b}{\sqrt{Re_\phi}} = 1.40\,\mathrm{mm}. \tag{8}$$

2.2 Solution Method

The commercial CFD package ANSYS Fluent was used to carry out the fluid domain only LES simulations of the rotating cavity. Face values of the solver variables were interpolated using a second order upwind scheme, and velocity and pressure were coupled using the SIMPLEC algorithm. We did not

Table 1. Rotating cavity dimensions and operating conditions.

Parameter	Description	Value
r_s	Shaft radius	0.12 m
a	Cob radius	0.138 m
b	Shroud radius	0.4 m
s	Cavity axial width	0.08 m
Re_z	Axial Reynolds number	3×10^3
Re_ϕ	Rotational Reynolds number	8×10^5
$\beta\Delta T_{max}$	Buoyancy parameter	0.27
Ω	Cavity angular velocity	56.67 rad/s
T_{in}	Throughflow temperature	298.15 K
T_{max}	Maximum wall temperature	378.15 K

use an explicit sub-grid scale (SGS) model; instead, the dissipation inherent in the second order upwind scheme was used to approximate unresolved scales of the flow. This approach has the benefit of avoiding the contamination of laminar flow structures by SGS viscosity [17], and has been successfully used in rotating cavities before - e.g. by Onori et al. [18]. The power spectral density of the velocity fluctuations was inspected at the centre of the cavity. The presence of a -5/3 region was confirmed and we did not observe a build of up energy at high frequencies, indicating sufficient numerical SGS dissipation in our simulations.

For the fluid domain only simulations, the temperatures on the disks were set to radially vary in the same way as the experimentally measured disk temperatures in Bohn et al. [16]. As no shroud temperature was available, this was set to the average of the two experimental disk temperatures at maximum radius. The inlet total pressure (with zero swirl) was adjusted to match the experimental value of Re_z (Tab. 1), and a static pressure condition was used on the outlet. The flow at the inlet was considered to be laminar due to the low axial Reynolds number. The inlet and outlet are extended compared to the experiment to allow the velocity profile to develop and prevent reverse flow at the boundaries. The fluid density was determined from the temperature and pressure using the ideal gas equation, and a temperature dependent dynamic viscosity and thermal conductivity were used. Radiation

effects were not included.

2.3 Baseline LES Verification and Validation

We define a Nusselt number (based on the wall heat flux q_w and radial coordinate r) as

$$Nu = \frac{q_w r}{k_{in}\left(T_w - T_{\text{in}}\right)}. \tag{9}$$

This is more of a convenient normalised heat-flux rather that a true Nusselt number, as it does not represent the ratio of heat transfer by convection and conduction. To ensure that our computational approach for the fluid domain is valid and that our conclusions are mesh independent, we compare the time- and circumferential-average Nusselt number to experimental data for three fully hexahedral meshes: a coarse 2.4M cell mesh, a medium 5.1M cell mesh, and a fine 10.2M cell mesh. The 5.1M cell and the 10.2M cell simulations were initialised from the solution on the coarser mesh and run for 30 revolutions to remove the initial transient, before being run for a further 30 revolutions to gather time-independent statistics.

This comparison is shown in Fig. 2. In general, the disk heat transfer matches the experimental data well, and is quite insensitive to the mesh resolution. At low radii ($r/b < 0.6$, where r is the radius) on the upstream disk, the 2.4M cell mesh gives a consistently lower Nusselt number, whilst this is almost identical between the 5.1M cell and 10.2M cell mesh. As it gives similar disk heat transfer to a significantly finer mesh for a much smaller mesh count, we use the 5.1M cell mesh for all other fluid domains in this paper.

The 5.1M cell mesh has a wall-normal spacing of $0.15\,\text{mm} \approx 0.1\delta_{\text{Ek}}$. This wall normal spacing gives an average z^+ of 1.26 on the disks, and an average r^+ of 0.72 on the shroud. This gave average cell aspect ratios (wall-normal spacing divided by the square root of the cell face area on the wall) of 22 on the disks and 17 on the shroud, inline with previous wall resolved LES investigations on rotating cavities [1] and common LES resolution requirements [19]. 240 time-steps are used per revolution of the cavity, giving an volume-average convective CFL number of 0.4.

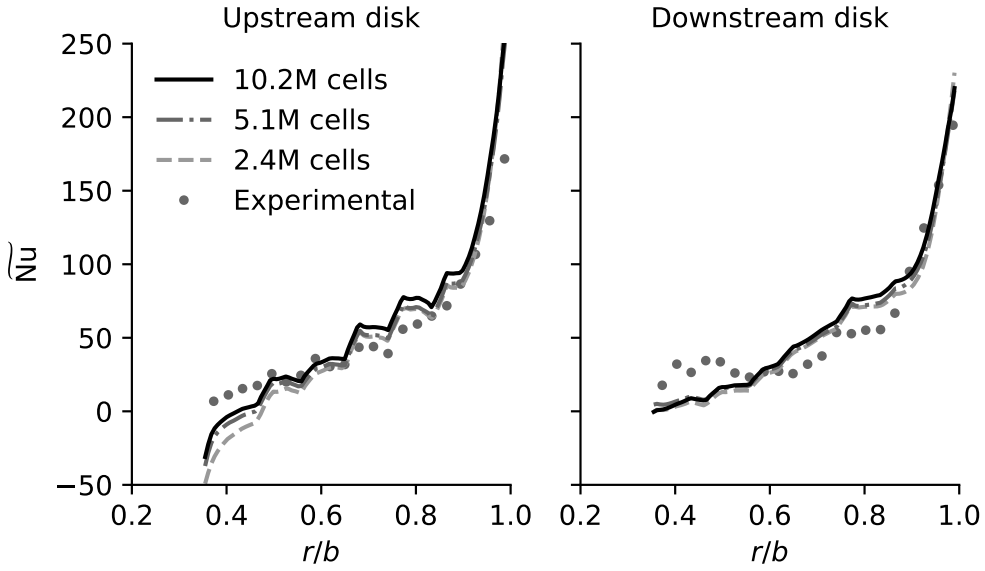

Fig. 2. Average disk Nusselt number. Experimental data from [16].

2.4 Near-Disk Thermal Unsteadiness

The normalised temperature, calculated by

$$T^* = \frac{T - T_{\text{in}}}{T_{\text{max}} - T_{\text{in}}}, \tag{10}$$

is shown in Fig. 3 on the axial mid-plane ($z/s = 0$) for the 5.1M cell mesh. The three regions of radial outflow caused by the large-scale counter-rotating circulation pairs (with cyclonic and anti-cyclonic circulations denoted by $-\Delta p$ and $+\Delta p$ respectively) can be seen to have a significantly lower temperature than the radial inflow. This flow structure rotates slightly slower than the cavity in the inertial frame of reference; in the cavity's frame of reference, this flow structure appears to rotate slowly against the direction of cavity rotation.

The slip of the large-scale flow structure causes a large low frequency temperature oscillation throughout the cavity. Of particular interest in this paper is the near-disk region, as this is critical for heat transfer and fluid-solid thermal coupling. Figure 4 shows the frequency spectrum of the temperature fluctuation a distance of 0.2 mm (well within the disk Ekman layer) from the downstream disk.

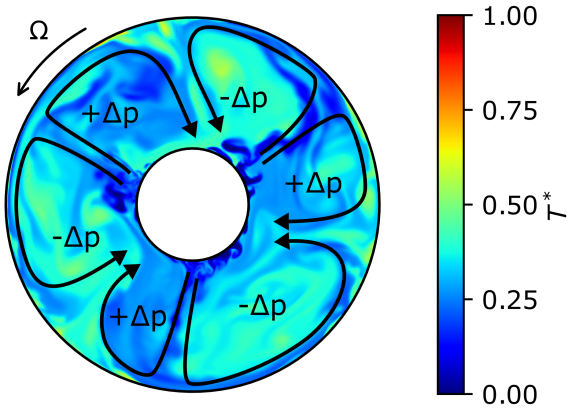

Fig. 3. Instantaneous values of temperature on the axial mid-plane.

There is a clear peak in the spectrum at

$$\frac{2\pi f_0}{\Omega} = 0.181. \tag{11}$$

The frequency of the spectral peak implies that, for the three radial arm flow structure seen in Fig. 3, the near-disk fluid is slipping at a rate of $0.181/3 = 6\%$ of the cavities angular speed. These observations are qualitatively consistent with other computational investigations of this cavity at different conditions [1].

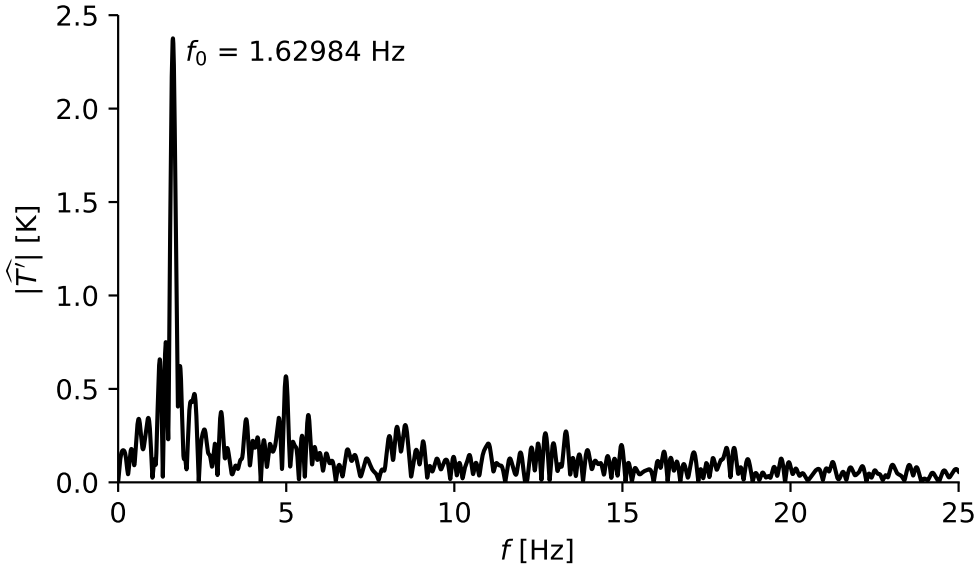

Fig. 4. Frequency spectrum of the near-disk temperature fluctuations.

As mentioned previously, the very low frequency fluctuation is a practical issue for carrying out LES-CHT in rotating cavities. If we consider a 5 mm thick titanium solid domain with a thermal diffusivity of $2.85 \times 10^{-6}\,\mathrm{m}^2/\mathrm{s}$, this temperature fluctuation would have a penetration depth of 3.4 mm - a significant distance into the solid domain. Therefore, to be consistent, it is desirable to develop a method that allows us to capture this frequency of unsteadiness without having the solution corrupted by errors in the initial solid-domain temperature field or by under-resolving the thermal penetration depth of higher frequencies.

3 Multi-Scale LES-CHT Solution Method

3.1 LES-CHT Challenges and Approach

Solving the fluid and solid domain together in a time consistent manner (i.e. with the same time-step) is extremely difficult. There are two reasons for this: the first is that the characteristic time-scale the solid domain is roughly 4 orders of magnitude larger than that of the fluid domain [10]. This is particularly an issue for getting past the initial transient in the solid times. The second reason is that under-resolving the thermal-penetration depth in the solid domain can risk over predicting the amplitude of the temperature fluctuations on the interface by one or two orders of magnitude [13]. This means that even though a certain frequency of fluctuation may not be dynamically relevant to the physics, if its penetration depth is under-resolved it could corrupt the entire flow field.

In many turbomachinery problems, the frequencies of the near-wall thermal unsteadiness are small enough so that they do not penetrate a significant distance in to the solid domain and can be reasonably modelled using the transfer function approach as in He [11] (Eq. 5 in this paper). However, the situation in rotating cavities is complicated by the existence of a very low frequency temperature fluctuation caused by the passing of the cold radial outflow and warm radial inflow.

The low frequency unsteadiness could be at a frequency where the penetration depth is larger than the solid domain thickness so that the temperature fluctuation on the fluid-solid interface interacts with the boundary condition on the other side of the disk. If this is the case, the unsteadiness needs to be solved in the solid domain to allow for the appropriate non-local interactions.

From the above discussion we can see three requirements for a multi-scale LES-CHT method that can be used to simulation rotating cavities:

1. The initial transient should be accelerated so that a quasi-steady state is reached without having to do an impractically long simulation.
2. Frequencies with a resolvable penetration depth should be solved in the solid domain. Present methods for LES-CHT do not allow for this, so we extend the approach of He [11] to enable the solution of low frequencies with a time-spectral solid domain.
3. Frequencies with a penetration depth that is too small to be resolved by the solid domain mesh should be solved using the wall transfer function approach as in [10, 11].

To meet these requirements, we solve for the time-mean (i.e. average) wall temperature by coupling to a steady solid solution, and solve for the unsteady wall temperature by either coupling to a time-spectral solid solved in the frequency domain (instead of the time domain) or using the wall transfer function approach [11]. Solving for the wall temperature fluctuations in the frequency domain makes it simple to separate scales between frequencies that need to be resolved because they penetrate a significant distance in to the solid domain and frequencies that can be solved for using the wall transfer function. The derivation and implementation of this method is outlined below.

3.2 Time-Spectral Solid Domain Solution

Starting with with the general equation for unsteady heat conduction,

$$\frac{\partial}{\partial t}\left(\rho c T\right) = \nabla \cdot \left(k \nabla T\right), \tag{12}$$

we decompose the unsteady temperature and fluid properties in the solid domain into their time-average and fluctuating components so that, for a generic variable ψ,

$$\psi = \widetilde{\psi} + \psi'. \tag{13}$$

This decomposition can be substituted in to Eq. 12 to obtain two separate equations for the steady temperature and the temperature fluctuations.

Assuming that the solid thermal properties are only dependent on the mean temperature (i.e. $\rho_s', c_s', k_s' =$

0), the equation for the steady solid domain temperature becomes

$$\frac{\partial \widetilde{T}}{\partial \tau} + \nabla \cdot \left(\widetilde{k_s} \nabla \widetilde{T} \right) = 0, \tag{14}$$

this can be solved by pseudo-time-marching in τ at a large but stable time-step to eliminate the long initial transient provided that suitable time-average boundary conditions are available [11].

The equation for the temperature fluctuation, T', in the solid domain is

$$\frac{\partial}{\partial t} \left(\widetilde{\rho} \widetilde{c} T' \right) = \nabla \cdot \left(\widetilde{k} \nabla T' \right). \tag{15}$$

T' can be expressed using an N harmonic Fourier expansion with a base frequency of ω_0 as

$$T'(t) = \sum_{n=1}^{N} A_n \cos(n\omega_0 t) + B_n \sin(n\omega_0 t). \tag{16}$$

Combining these two equations, and evaluating the resulting equation at two phase angles ($n\omega_0 t = 0$ and $n\omega_0 t = \pi/2$) gives the governing equations for a time-spectral solid domain at frequency $n\omega_0$:

$$\begin{cases} \dfrac{\partial A_n}{\partial \tau} = \nabla \cdot \widetilde{k} \nabla A_n - n\omega_0 \widetilde{\rho} \widetilde{c} B_n \\ \dfrac{\partial B_n}{\partial \tau} = \nabla \cdot \widetilde{k} \nabla B_n + n\omega_0 \widetilde{\rho} \widetilde{c} A_n \end{cases}. \tag{17}$$

Similarly to the steady solid domain equation (Eq. 14), these equations can be solved by pseudo-time-marching in the time-spectral domain. Again, these equations remove the need to simulate the solid domain initial transient provided that suitable harmonic boundary conditions are available. As A_n and B_n do not appear in the equation for the time-average solid domain or in the equations for other frequencies in the time-spectral solid domain, an arbitrary number of harmonics can be used depending on what is needed to capture the spectral content of the fluid domain.

Solving an unsteady solid-domain in this manner was proposed by He and Oldfield [10], and has been used to do unsteady CHT by Mehdizadeh et al. [20] with a non-linear harmonic (NLH) solver that solved the fluid in the frequency domain. NLH approaches are unsuitable for use in LES, so a method of interfacing a time-spectral solid and time-marching fluid is needed.

3.3 Fluid-Solid Interface Treatment

The two conditions that need to be satisfied on the fluid-solid interface are the conservation of heat-flux ($q_f + q_s = 0$), and the continuity of temperature. Using a local 1D expression for between the fluid and solid cell centres on either side of the interface (at temperatures T_f and T_s respectively) and the wall (at T_w), this gives

$$h_f \left(T_f - T_w\right) = h_s \left(T_w - T_s\right), \tag{18}$$

where $h_f = k_f/\Delta x_f$, $h_s = k_s/\Delta x_s$, and Δx is the distance from the cell centre to the wall.

Time-average solid domain: Substituting the decomposition in Eq. 13 into Eq. 18 and averaging gives the interface condition for time-average temperature on the fluid-solid interface as

$$\widetilde{T_w} = \frac{\widetilde{h_f T_f} + \widetilde{h}_s \widetilde{T}_s - \widetilde{h'_f T'_w}}{\widetilde{h}_f + \widetilde{h}_s}. \tag{19}$$

This boundary condition is used for the time-average solid domain and to reconstruct the unsteady wall temperature that is supplied to the fluid domain. It is worth noting that the effect of the fluid domain thermal conductivity temperature dependence on the time-average heat flux is included in this boundary condition, although in most cases it is not expected to have a significant influence. The averages of the fluid-side terms in Eq. 19 are obtained at time step $M+1$ through a simple recursive moving average:

$$\widetilde{\Psi}_{M+1} = \frac{1}{M+1}\Psi_{M+1} + \frac{M}{M+1}\widetilde{\Psi}_M. \tag{20}$$

Time-spectral solid domain: Using the substitution of Eq. 13 into Eq. 18, and neglecting the effect of thermal conductivity fluctuations on the temperature fluctuations, we can also derive an expression for the temperature fluctuation on the interface as

$$T'_w = \frac{\widetilde{h_f} T'_f + \widetilde{h_s} T'_s}{\widetilde{h_f} + \widetilde{h_s}}. \tag{21}$$

To use this as a boundary condition for the time-spectral solid domain, we substitute in the Fourier decomposition for the temperature fluctuation T' (Eq. 16) to get a harmonic balance boundary condition for the the time-spectral domain:

$$\begin{cases} A_w = \dfrac{\widetilde{h_f} A_f + \widetilde{h_s} A_s}{\widetilde{h_f} + \widetilde{h_s}} \\ B_w = \dfrac{\widetilde{h_f} B_f + \widetilde{h_s} B_s}{\widetilde{h_f} + \widetilde{h_s}} \end{cases}. \tag{22}$$

The fluid-side Fourier coefficients are calculated through a recursive discrete Fourier transform (DFT) in a similar manner to the moving average:

$$\begin{cases} \left[A_{f,n}\right]_{M+1} = \dfrac{2}{M+1} \cos(n\omega_0 t) \left[T'_f\right]_{M+1} + \dfrac{M}{M+1} \left[A_{f,n}\right]_M \\ \left[B_{f,n}\right]_{M+1} = \dfrac{2}{M+1} \sin(n\omega_0 t) \left[T'_f\right]_{M+1} + \dfrac{M}{M+1} \left[B_{f,n}\right]_M \end{cases}. \tag{23}$$

To use the transfer function approach when the solid domain mesh is not sufficient to resolve the thermal penetration depth of the frequency $n\omega_0$, the complex Fourier harmonics of the temperature fluctuation can be expressed as $\widehat{T'}_n = A_n - iB_n$. This can then be used with Eq. 5 to calculate the wall temperature fluctuation with the wall transfer function approach.

The choice of ω_0 and n is problem dependent: in general one would choose ω_0 to be the lowest periodic frequency present in the temperature signal, and choose n according to the number of spectral peaks to ensure a good reconstruction of the relevant scales of the temperature fluctuations. For example,

in Fig. 4, we choose $\omega_0 = 2\pi f_0$ and $n = 1$.

Unsteady fluid domain: The unsteady time-domain temperature supplied to the fluid domain can simply be reconstructed from Eqs. 19 and 22 as

$$T_w = \widetilde{T_w} + \sum_{n=1}^{N} A_{w,n}\cos(n\omega_0 t) + B_{w,n}\sin(n\omega_0 t). \tag{24}$$

3.4 Implementation in Commercial CFD Software

The new LES-CHT method is implemented as a monolithic method in ANSYS Fluent using the user defined function (UDF) programming interface and Scheme solver macros. This flow solver is a common part of the tooling in both academic and industrial internal air systems communities. Having the fluid and solid domains in the same solver process leads to simpler interface conditions, better data locality, and no need to write additional inter-solver communication code [11].

Being a component of a closed-source commercial software package, UDFs only allow high-level access to the workings of the solver and do not allow changes to its architecture. This indicates the ease of implementation of the proposed methods. An additional benefit of implementing the methodology in an established flow solver is the potential for straight forwards integration of other models (such as wall modelling, radiation, or combustion) in future investigations.

The general solution process is as follows:

1. Time march the fluid with time-step Δt_f and the solid with time-step $\Delta t_s \gg \Delta t_f$ to get past the initial transient.
2. Initialise the moving averages and DFT.
3. March the steady and the time-spectral solid domains in pseudo-time and the fluid domain in physical time. At the end of each time-step, update the moving average (Eq. 20) and DFT (Eq. 23).
4. At the start of the next time-step use Eqs. 19, 22, and 24 to calculate the boundary conditions for the time-average solid domain, time-spectral solid domain, and time-marching fluid domain.

4 LES-CHT Simulations

4.1 Case Information

To investigate the sensitivity of the cavity aerodynamics to its heating configuration, we couple the fluid to a 5 mm thick solid domain (the same thickness as the plastic disks in Bohn et al. [16]) using the LES-CHT method outlined in the previous section. The location of the fluid-solid interfaces on the disks, cobs, and shroud can be seen if Fig. 1. The thickness of the solid domain is resolved by 10 mesh cells. We consider two different combinations of solid domain external boundary conditions and materials: axial heating with a low conductivity material (Fig. 5a), and radial conduction with a higher conductivity material (Fig. 5b). It is worth highlighting that both of these cases have the same bulk description in terms of Re_z, Re_ϕ, and $\beta\Delta T_{max}$ as the baseline LES case.

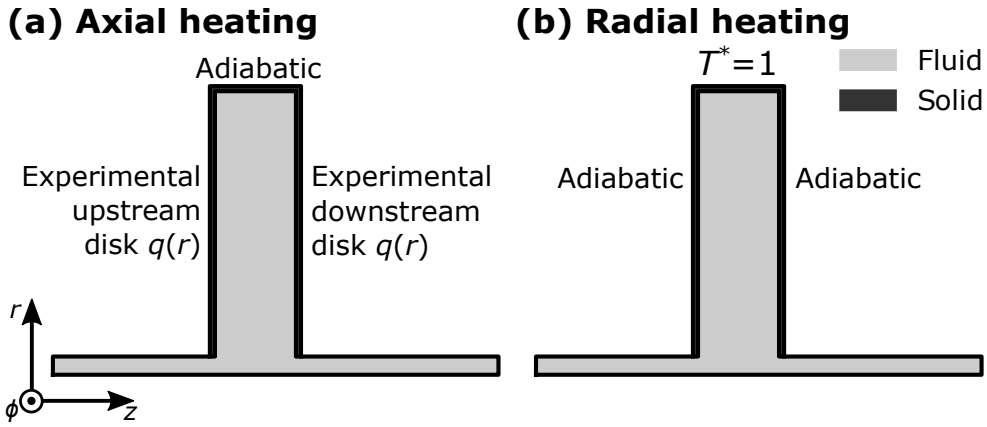

Fig. 5. Solid domain external boundary conditions for the axial and radial heating configurations.

Axial heating: For this case, heat fluxes calculated from the experimental Nusselt number and temperature in [16] are applied to the exterior of the solid disks, and an adiabatic boundary condition is applied to the exterior of the shroud (corresponding to the unheated shroud in [16]) as in Fig. 5a. Our intention with this case was to replicate the experimental configuration in [16] as best as we were able - although inevitably some simplifications to the solid domain geometry were made. This configuration is also similar to other experimental studies on rotating cavities [21,22]. In keeping with the experiment of Bohn et al., we use epoxy as the material for the solid domain. For the epoxy material properties used, see Tab. 2. The thermal penetration depth for the frequency of unsteadiness from Fig. 4 in epoxy disks is 0.8 mm - this is not even two mesh cells wide, so our epoxy solid domain is not able to accurately resolve this frequency of unsteadiness. We therefore use the 1D semi-infinite wall transfer function to

calculate the wall temperature fluctuations for this case.

Radial heating: This case is more representative of how a rotating cavity would be heated in an aero-engine compressor. The exterior of the solid domain at the shroud is set to a temperature of $T_{\max} = 378.15\,\mathrm{K}$ (i.e. $T^* = 1$), and exterior of the disks have an adiabatic condition s in Fig. 5b. For this case, the solid domain uses the thermal properties of Titanium (Tab. 2). The thermal penetration depth for the frequency of unsteadiness from Fig. 4 for titanium disks is 3.4 mm - this a significant proportion of the disk thickness, so we use the time-spectral solid domain for this case.

4.2 Solution process

All LES-CHT cases proceeded by time-marching both domains in a desynchronised fashion with $\Delta t_s = 10,000\Delta t_f$ for 30 revolutions to get through the initial transient. Then, 10 revolutions of this desynchronised time-marching were used to calculate a values to initialise the moving average and DFT with. Data gathered from numerical sensors placed near the disks in this period was used to calculate a value for ω_0 for the DFT and time-spectral solid domain. Only one Fourier harmonic (at ω_0) was used with the wall transfer function or time-spectral solid domain.

The boundary conditions were then changed to the time-mean and harmonic balance conditions and the flow was solved for 20 revolutions. A pseudo time-step of $10,000\Delta t_f$ was used for the time-mean solid domain, and a pseudo time-step of $100\Delta t_f$ was used for the time-spectral domain. Finally flow-field statistics were collected for a further 30 revolutions.

Table 2. Solid domain thermal properties.

Property	ρ [kg/m^3]	c [J/kgK]	k [W/mK]
Epoxy	1200	1000	0.2
Titanium	4500	570	7.3

The value for the solid time-step Δt_s in the initial steps of the solution process was chosen to approximately equalise the characteristic fluid and solid time-scales as discussed earlier. As we use implicit time-stepping, there are not any stability considerations for choosing Δt_s, if explicit time-stepping was to be used then Δt_s would be chosen to be as large as possible while preserving stability.

4.3 LES-CHT Results

The time- and circumferentially-averaged disk temperatures and Nusselt numbers from the CHT simulations are shown in Fig. 6.

The average disk temperature for the axially heated case matches reasonably well with the experimental data considering that we were not able to exactly replicate the experimental solid domain geometry. The agreement between the experimental Nusselt number and the Nusselt number from the axially heated case is near perfect.

The disk temperatures calculated for the cavity heated by radial conduction are substantially different to the axially heated case - they drop rapidly at high radii and then more shallowly at low radii. The disk Nusselt numbers for the radially heated case are also consistently lower than the axially heated case.

On the shroud, Fig 7 shows a substantial difference in the thermal behaviour of the two cases. For the axially heated case, the shroud temperature is low due to the low thermal conductivity of the solid domain, and the Nusselt number drops significantly towards the mid-axial location $z/s = 0$. For the case heated by radial conduction, the shroud temperature is uniform and close to $T_{\max}$, and the Nusselt number does not have the large variation present in the axially heated case.

Instantaneous temperatures and radial velocities on the axial mid-plane ($z/s = 0$) from the two cases are shown in Figs. 8 and 9. Both cavities have the same three circulation pair large-scale flow structure. The temperature contrast between the radial inflow and outflow is smaller for the axially heated case (Fig. 8a) than the radially heated case (Fig. 8b), despite the significantly hotter disks in the former. Comparing Fig. 9a and Fig. 9b, the radial out/inflow in the axially heated case is less intense than in the radially heated case - this is consistent with the flow being buoyancy driven and the smaller temperature differential between the cold outflow and warm inflow observed in Fig. 8.

The Fourier harmonics of the wall temperature fluctuation (A_w and B_w) for the axially heated case are shown in Fig. 10, for the radially heated case in Fig. 11. Note that, due to the difference in the thermal conductivities of epoxy and titanium, the colour map in Fig. 10 covers a range ten times larger than the colour map in Fig. 11. Apart from the expected difference in intensities between the two cases, it is interesting to note the regions of out-of-phase temperature fluctuation near the shroud - these extend to a lower radii in the axially heated case than they do in the radially heated case.

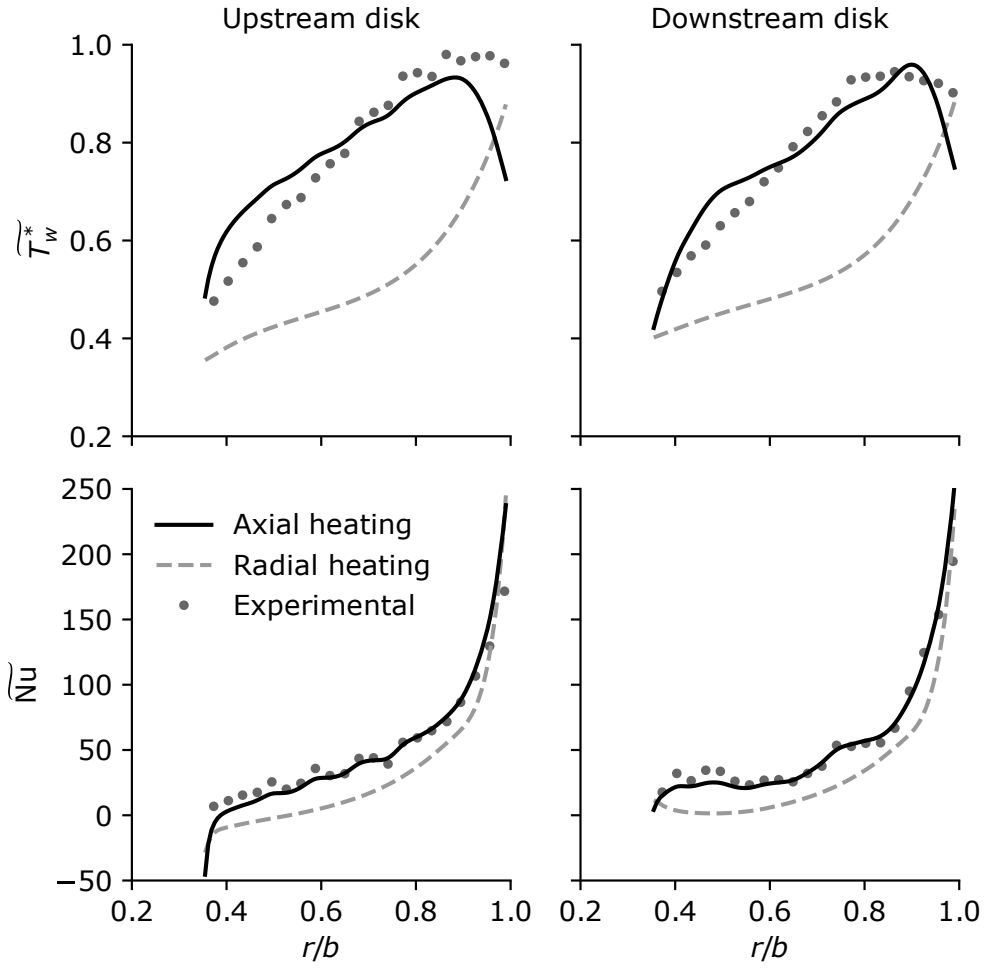

Fig. 6. Average disk temperature (top) and Nusselt number (bottom). Experimental data from [16]

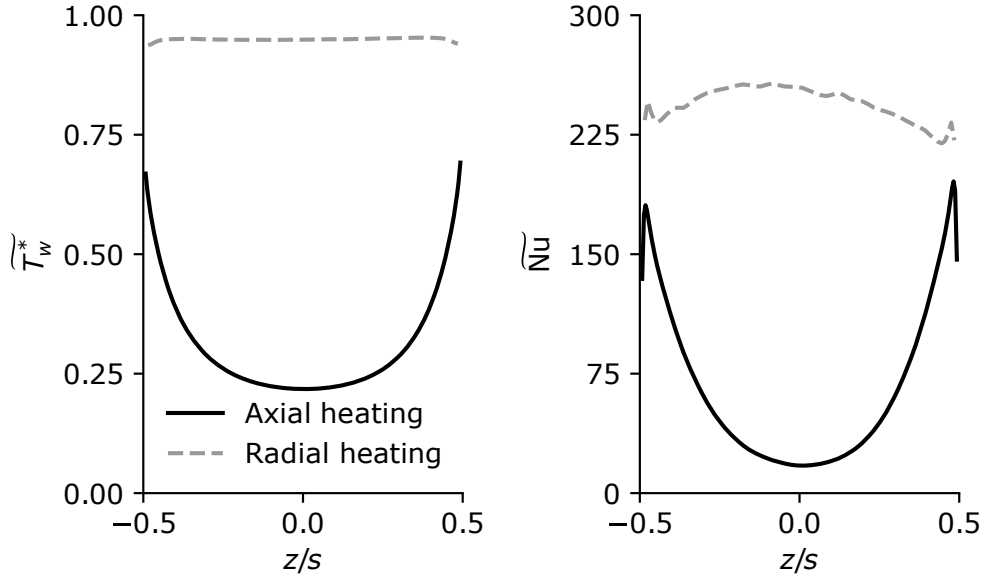

Fig. 7. Average shroud temperature (left) and Nusselt number (right).

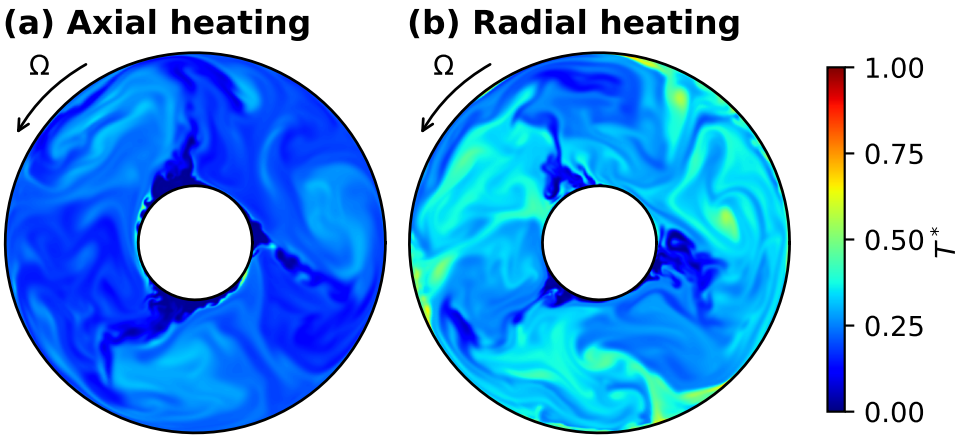

Fig. 8. Instantaneous LES-CHT mid-plane fluid temperatures.

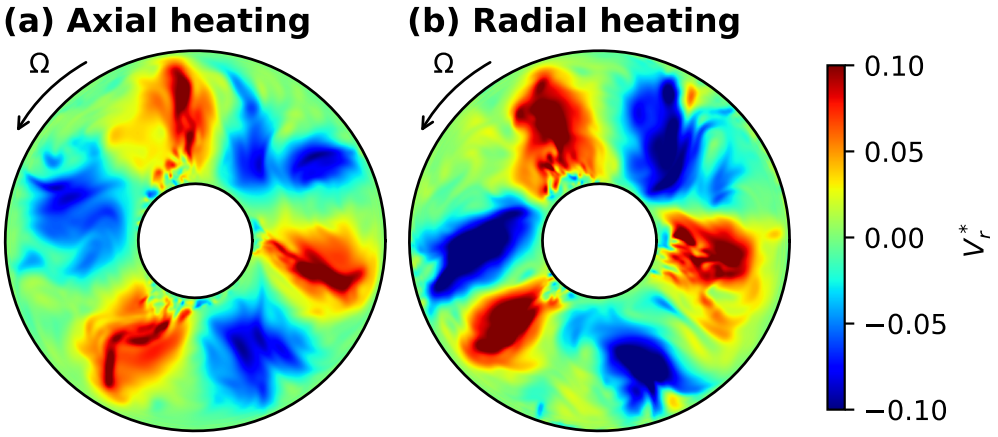

Fig. 9. Instantaneous LES-CHT mid-plane radial velocity.

5 Comparison of Axial vs. Radial Heating

The results in the previous section (Figs. 6 and 7) show that the disk and shroud temperatures and Nusselt numbers are dependent on the cavity heating configuration, and that the large-scale global flow structure remains qualitatively unchanged for both the axially heated and radially heated case. However, it is also possible that the local heating has an effect on the cavity aerodynamics and local small-scale flow structures that are important for predicting heat transfer. To investigate this, we now focus on the flow in two key areas (near the shroud and near the disk) to see if and how they are impacted by the different local heating condition.

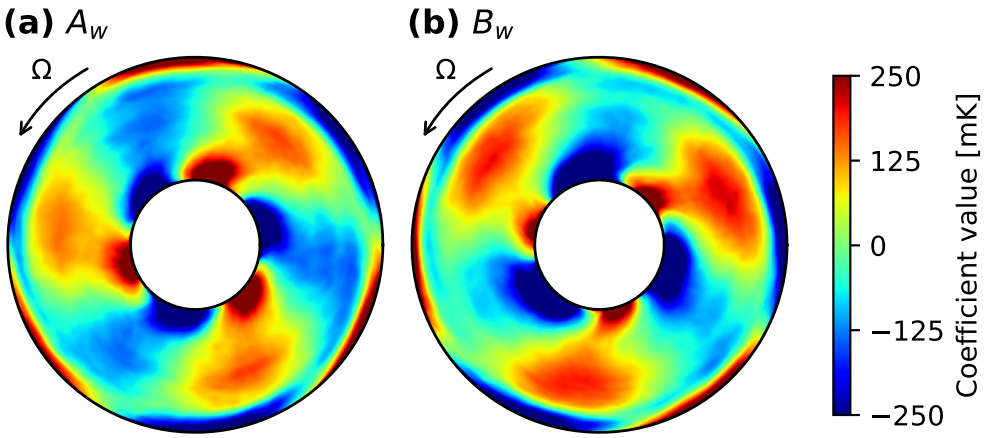

Fig. 10. Axially heated downstream disk wall temperature fluctuation harmonic coefficients.

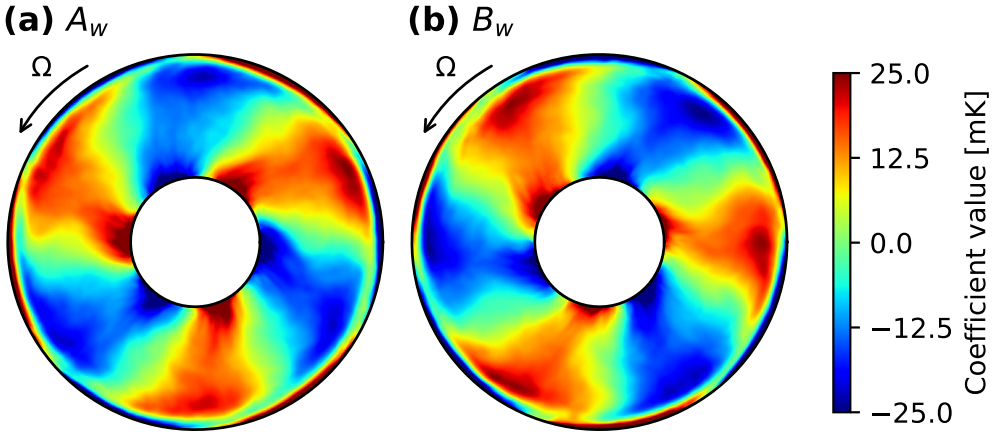

Fig. 11. Radially heated downstream disk wall temperature fluctuation harmonic coefficients.

5.1 Effect on Shroud Flow Structure

Figure 12 shows the instantaneous Nusselt numbers on the shroud and the downstream disk. Looking at the shroud, streaks of enhanced heat transfer are visible in the radially heated case (Fig. 12a), but not in the axially heated case. Referring back to the average shroud Nusselt numbers in Fig. 7, it can be seen that the occurrence of these streaks leads to a overall enhanced shroud Nusselt number.

The reason for the formation (or not) of these flow structures can be seen from average temperature contours in the fluid domain in Fig. 13. Even though both cavities appear to have similar axially averaged radial temperature distributions, the mixing of hot fluid from near the heated surfaces is quite different between the two cases.

Taking Fig. 13a together with the shroud temperature distributions in Fig. 7, it can be seen that the

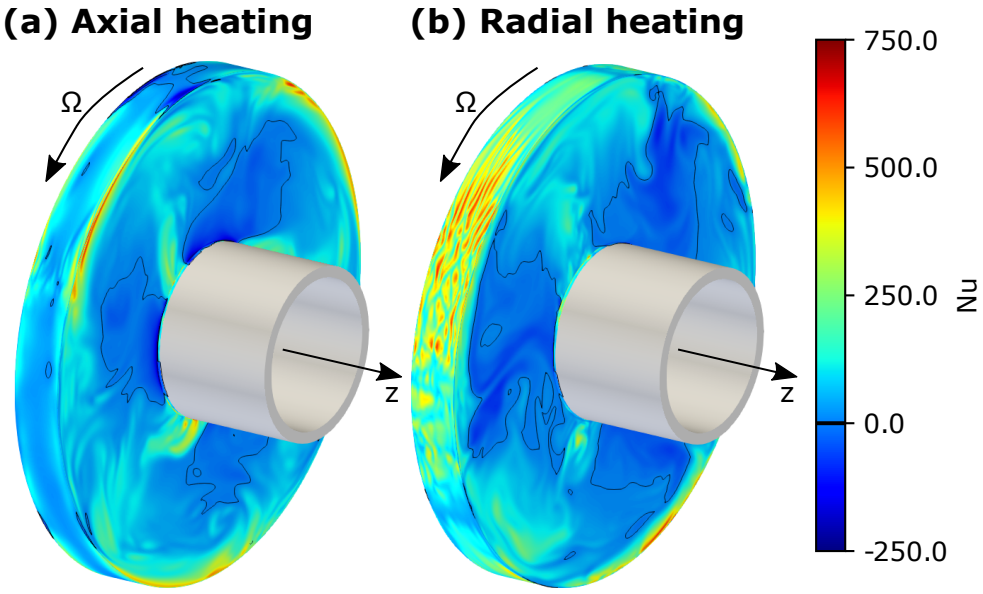

Fig. 12. Instantaneous Nusselt numbers on the shroud and downstream disk.

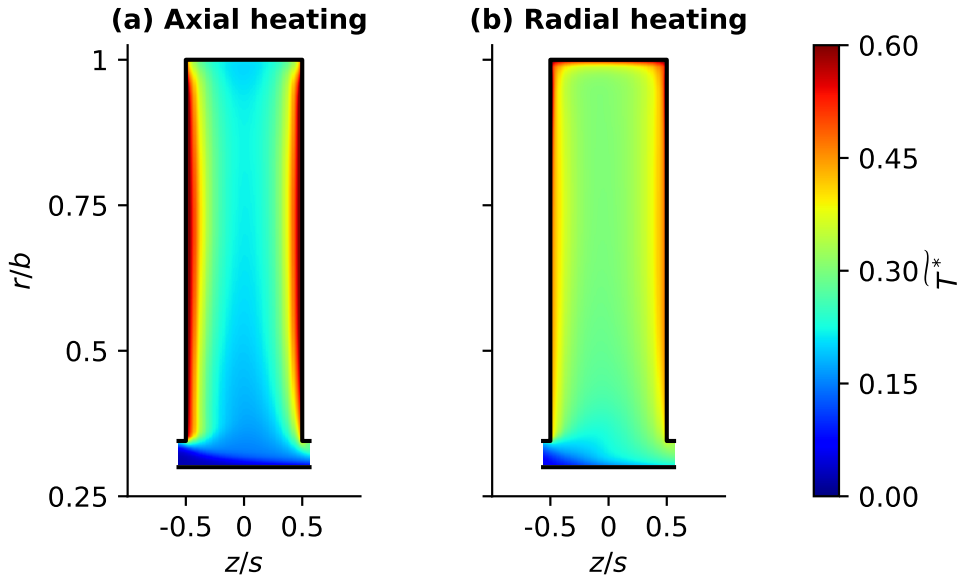

Fig. 13. Average static temperature in the meridional plane.

near shroud region for the axially heated case has a negligible radial temperature gradient, meaning that there is no buoyancy force driving the formation of the streaks as was observed in [1, 3, 4]. The shroud temperature is so low in this case due to the low thermal conductivity of the solid domain material - any shroud heat flux has to come via axial conduction from the outer radii of the disks, so even a small shroud heat flux causes a large temperature drop relative to the temperature at the top of the disks (Fig. 6).

In contrast, the radially heated disks have an unstable near-shroud radial density gradient that causes

the formation of the streaks (particularly in the cyclonic circulations) that enhance heat transfer by mixing the colder fluid in the bulk flow with the hotter fluid near the shroud in a manner consistent with Rayleigh-Bernard convection, as in Puttock-Brown et al.'s papers [3, 4].

The effect of the difference in shroud flow structure is not restricted to the near-shroud region of the flow. Heat transfer from the disks is much less efficient than heat transfer from the shroud at mixing fluid from the local heated surface with the bulk flow. This can be observed in Fig. 13a, where the high temperatures in the axially heated case are very much restricted to the near-disk region, leading to colder mid-cavity flow. In contrast, the radially heated case in Fig. 8b exhibits a significantly warmer bulk flow due to the more efficient mixing of the hot fluid from the heated shroud by the streaks. This effect on the bulk flow can also be observed in the instantaneous temperature contours in Fig. 8, and the less intense radial arms in the axially heated case (see Fig. 9) can be attributed to the reduced buoyancy force caused by a smaller temperature differential between the cold axial throughflow and the warmer cavity fluid.

The relevance of these near-shroud flow structures to our research question is that their formation is dependent on the strength of the local heating at the shroud - a significant heat-flux is needed to create a sufficient radial density gradient to drive the formation of these streaks.

5.2 Effect on Disk Flow Structure

The difference in the disk Nusselt numbers between the two cases shown in Fig. 6 implies that it is also worth examining the near-disk flow field for differences in the local flow-structures.

The flow close to the disks is widely accepted as behaving as a laminar Ekman layer; this has been demonstrated for this cavity at a similar operating condition [1], and at conditions closer to engine relevance by [2]. However, the near-disk flow that is outside of the Ekman layer (i.e. further than $\delta_{\mathrm{Ek}}/s = 0.0176$ from the disk) is rarely investigated, even though it is responsible for supplying forcing to the Ekman layer dynamics and effectively providing the "thermal boundary conditions" at the outer edge of the Ekman layer.

Figure 14 shows the axial turbulent heat flux, $\widetilde{V_z'T'}$: this is the effective heat flux caused by the axial velocity fluctuations when time averaging the flow. Near the upstream disk ($z/s = -0.5$), a positive value of $\widetilde{V_z'T'}$ is caused by axial velocity fluctuations away from the disk being associated with an increase in temperature and an axial velocity fluctuation towards the disk being associated with a decrease in

temperature - this is consistent with unsteady flow structures enhancing transport from a hot disk to a cooler bulk flow. On the downstream disk ($z/s = 0.5$) negative values of $\widetilde{V_z'T'}$ are consistent with this same unsteady mixing of fluid between the disk and bulk flow. The extreme values in the region above $r/b \approx 0.95$ in Fig. 14 are caused by the interaction of the near-disk flow with the shroud, we restrict our discussion to the flow that is only affected by the disk and the bulk flow, i.e. $r/b < 0.95$.

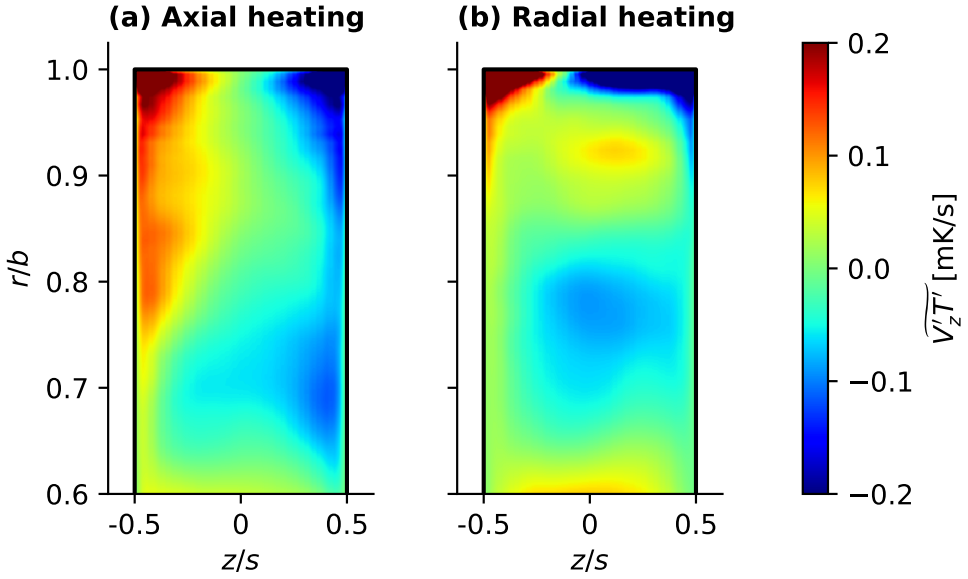

Fig. 14. Axial turbulent heat flux distribution in the meridional plane.

For the axially heated case (Fig. 14a), we see a turbulent heat flux near both disks that is not present for the radially heated case (Fig. 14b). Whilst the difference in $\widetilde{V_z'T'}$ is likely due to an increase in local flow structures mixing near-disk and bulk flow, it is possible that it is due to the higher temperature contrast between the disks and the bulk flow in the axially heated case increasing $\widetilde{V_z'T'}$ through an increase in the amplitude of T'.

To rule this out, the root-mean-square (RMS) velocity fluctuations were compared for the two cases by calculating a normalised difference as

$$\Delta V'_{z,\mathrm{RMS}} = \frac{\mathrm{RMS}\left(V'_{z,}\right)_{\mathrm{AH}} - \mathrm{RMS}\left(V'_{z}\right)_{\mathrm{RH}}}{\mathrm{RMS}\left(V'_{z}\right)_{\mathrm{RH}}}, \tag{25}$$

where AH and RH stand for the axially and radially heated cases respectively. The result of this compar-

ison is shown in Fig. 15: the axial velocity fluctuations are significantly larger ($\sim 25\%$) near the disks in the axially heated case, indicating the formation of turbulence or instabilities in this region caused by the disk heat transfer. Due to asymmetries in the axially averaged flow (see [1] and Fig. 14) this region is larger in the axially heated case (Fig. 15).

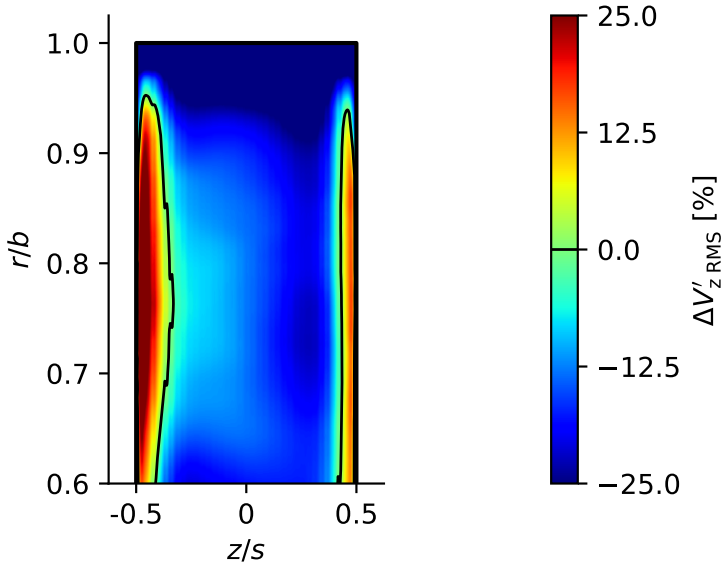

Fig. 15. Difference in disk-normal velocity fluctuation levels between the axially heated cavity and the radially heated cavity.

To visualise the flow structures causing the extra disk-normal mass and energy transport, Fig. 16 plots the radial vorticity $2\delta_{\mathrm{Ek}}$ from the upstream disk for both cases at the same time instant as Fig. 8a and Fig. 9a. This axial location is outside of the Ekman layer thickness, but still near-enough the disk so that flow structures that form here could affect the dynamics of the Ekman layer.

By comparing the values of the radial vorticity in Fig. 16a with those in Fig. 16b, the existence of radially aligned vortices forming in the anti-cyclonic circulation is clear in former, but not in the latter. This is indicative of the formation of some local large-scale turbulent or other coherent flow structures. The enhanced mixing of the near-disk and bulk flow through these flow structures may contribute to the higher Nusselt number observed in the axially heated case in Fig. 6. The contrast between Fig. 16a and Fig. 16b is quite start, and to the best of our knowledge this heating induced destabilisation and formation of vortices in the near-disk flow is not something that has been observed before. The mechanism for this warrants further investigation and is examined in detail below.

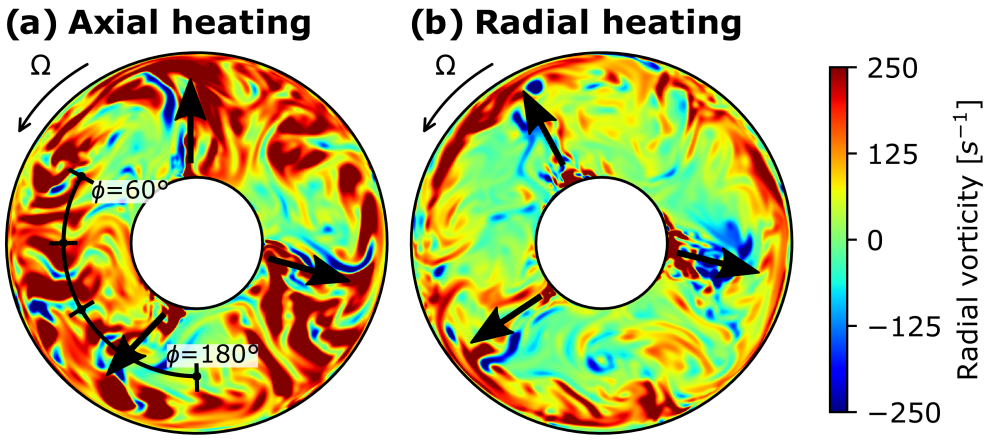

Fig. 16. Radial vorticity on the plane $2\delta_{\mathrm{Ek}}$ from the upstream disk ($z/s = -0.465$). Arrows indicate regions of radial outflow.

6 Heating Induced Near-Disk Instability

6.1 Behaviour of the Near-Disk Vortices

The positive sign of the vorticity in the structures in Fig. 16a is consistent with the vortices rolling up in the near-disk shear layer caused by the tangential slip of the large-scale flow structure. It makes sense that these vortices only form in the case with strong disk heating because, in air, the increased temperature in the near-disk fluid acts to destabilise the near-disk flow through the combined effects of the temperature dependent density and dynamic viscosity [23, 24]. However, this does not explain why the vortices seem to occur predominately in the cyclonic circulations.

The flow field for one circulation pair is shown on a radial isosurface of $r/b = 0.7$ in Fig. 17. The radial location for this plot is shown in Fig. 16a by a black line, with markers at 30° increments. The tangential coordinate ϕ is set to be zero at top dead-centre, and increases in the anti-clockwise direction. The distribution of radial vorticity in Fig. 17e shows that the vortical flow structures are confined to the near-disk region, and appear to form in the region of radial outflow ($\phi \approx 145°$ in Fig. 17b). Near the upstream disk, the vortices are rotating in the positive sense (consistent with Fig. 16b), and they rotate in the opposite direction near the downstream disk. Due to the globally negative tangential velocity (i.e. in the anti-cyclonic direction) visible in Fig. 17c, the vortices are observed to be present throughout the anti-cyclonic circulation. The vortices are not present in the cyclonic circulation as can be seen for $\phi > 150°$ in Fig. 17e - this implies that they are destroyed in the radial inflow just as they are generated in the radial outflow.

Figure 18 shows a zoomed in view of the region indicated with a dotted line in Fig. 17, with the

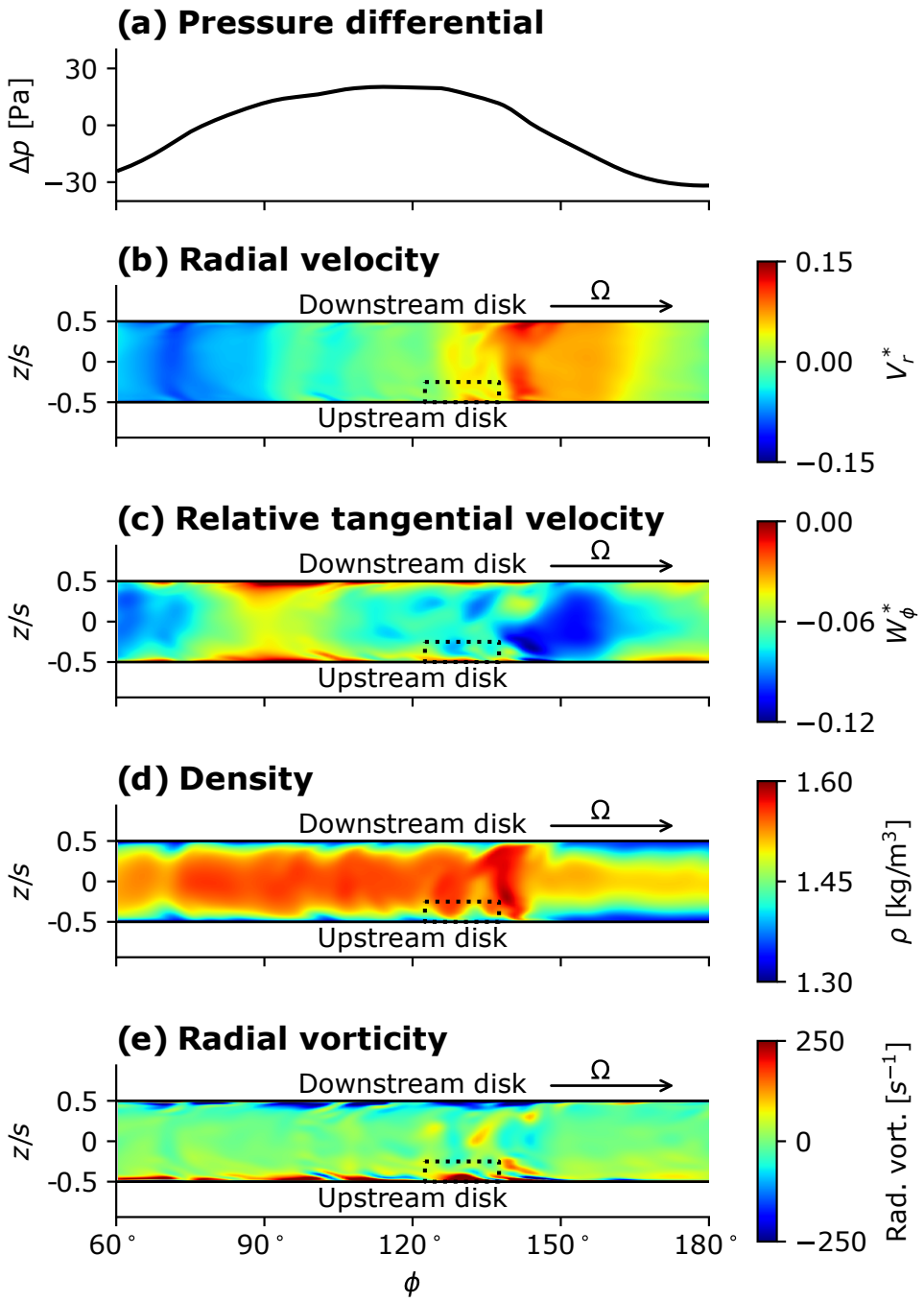

Fig. 17. Flow field in the ϕz-plane at $r/b = 0.7$ for the axially heated case. Circumferential location indicated in Fig. 16a.

distance from the wall (Δz) normalised by the theoretical laminar Ekman layer thickness, δ_{Ek}. The instability that causes these vortices originates at the wall within the Ekman layer. This can be seen in the circulation visible around $\phi \approx 130°$ in Fig. 18a, which extends up to about 2 Ekman layer thicknesses from the wall. From the temperature contours in Fig. 18a it would appear that this flow structure is not responsible for much wall-normal energy transport, however this is not the case. The flow structure is better visualised by subtracting the "large-scale" velocity (calculated by circumferentially averaging the

velocities over the plot area) from local relative velocities to calculate a velocity perturbation as shown in Fig. 18b. Here, we can clearly see a vortex that extends up to 10 Ekman layer thicknesses from the disk, ejecting hot fluid in to the bulk flow and injecting cold fluid into the near-disk region.

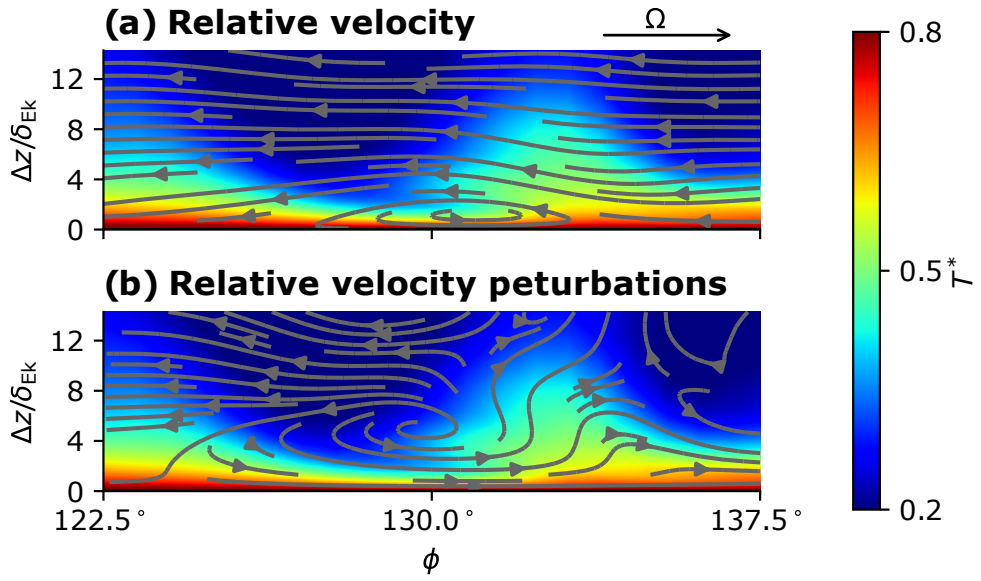

Fig. 18. Near disk instantaneous streamtraces and temperature showing a heating induced vortex. The region corresponding to this figure is outlined with dots in Fig. 17.

6.2 Heating Induced Destabilisation Mechanism

Figure 19a summarises the observations made in Fig. 17 and Fig. 18. Vortices are generated in the regions of radial outflow, destabilising the near-disk flow downstream in the cyclonic circulation, before being destroyed in regions of radial inflow.

The mechanism for the generation of vortices in the radial outflow is explained in the diagram of a single vortex near the upstream disk (Fig. 19b): in the radial arm, there is an adverse pressure gradient (see Fig. 17a), leading to a pressure force acting in the cyclonic direction on a fluid parcel. In the bulk flow, this is balanced by the Coriolis force from the radial outflow acting in the anti-cyclonic direction due to the positive radial velocity. Near the disk, the local heating causes a reduction in density (as seen in Fig. 17d), and hence a reduction in the local Coriolis force (which is proportional to density). This means that there is a net force acting in the cyclonic direction on the near-wall fluid, against the direction of the bulk flow. The net force acting against the direction of bulk flow drives the roll-up of a vortex with positive vorticity on the upstream disk, and a vortex with negative vorticity on the downstream disk

- this is consistent with the flow field shown in Fig. 17e.

The same logic can be used to explain the destruction of vortices in the radial inflow. As shown in Fig. 19c, the pressure force acts in the anti-cyclonic direction, stabilising the flow, and the Coriolis force acts in the cyclonic direction. Again, in the bulk flow, these forces are balanced, but in the near-disk region the Coriolis force is reduced due to the lower density; this gives a net force in the anti-cyclonic direction - this is in the same direction as the bulk flow, and opposes the sense of rotation of the vortices that are entering the region of radial inflow from the anti-cyclonic circulation.

6.3 Implications for Rotating Cavity Investigations

The heating induced destabilisation of the near-disk flow also has implications for studies that consider the bulk conditions where an Ekman layer may transition to turbulence, such as [6]. The result suggests two things: first, that the effect of wall heating may need to be taken in to account for Ekman layer transition considerations; and second, that these studies may need to be at a finer-grained than just considering bulk parameters to describe the flow - whether the Ekman layer will transition could be dependent on the local thermal boundary conditions.

These results also show that there are scenarios where the laminar Ekman layer modelling argument is an oversimplification when considering rotating cavity flows from a heat transfer perspective. A laminar Ekman layer would suggest that there are no self-generated flow structures causing wall-normal transport. Although this may be the case within the Ekman layer thickness, we have observed flow structures outside of this that footprint on the flow within this region and disrupt its dynamics. Due to the slow slip of the large-scale flow structure, this means that there is no region of the near-disk flow that can be considered to persistently behave in a manner consistent with a laminar Ekman layer.

In Fig. 18, the Ekman layer thickness corresponds to a local normalised wall distance of $z^+ = 11$. In conventional turbulent boundary layers it is widely accepted that flow structures that significantly affect heat transfer can occur further out and on larger scales than this. We have shown that this is the case for rotating cavities too - the heating induced vortical structures extend past $z^+ = 100$ - and that proper consideration of the near-disk flow that occurs outside of the laminar Ekman layers is important - this is relevant to wall and SGS modelling strategies that will need to take care not to disrupt the formation of these instabilities by excessive damping from the eddy/SGS viscosity.

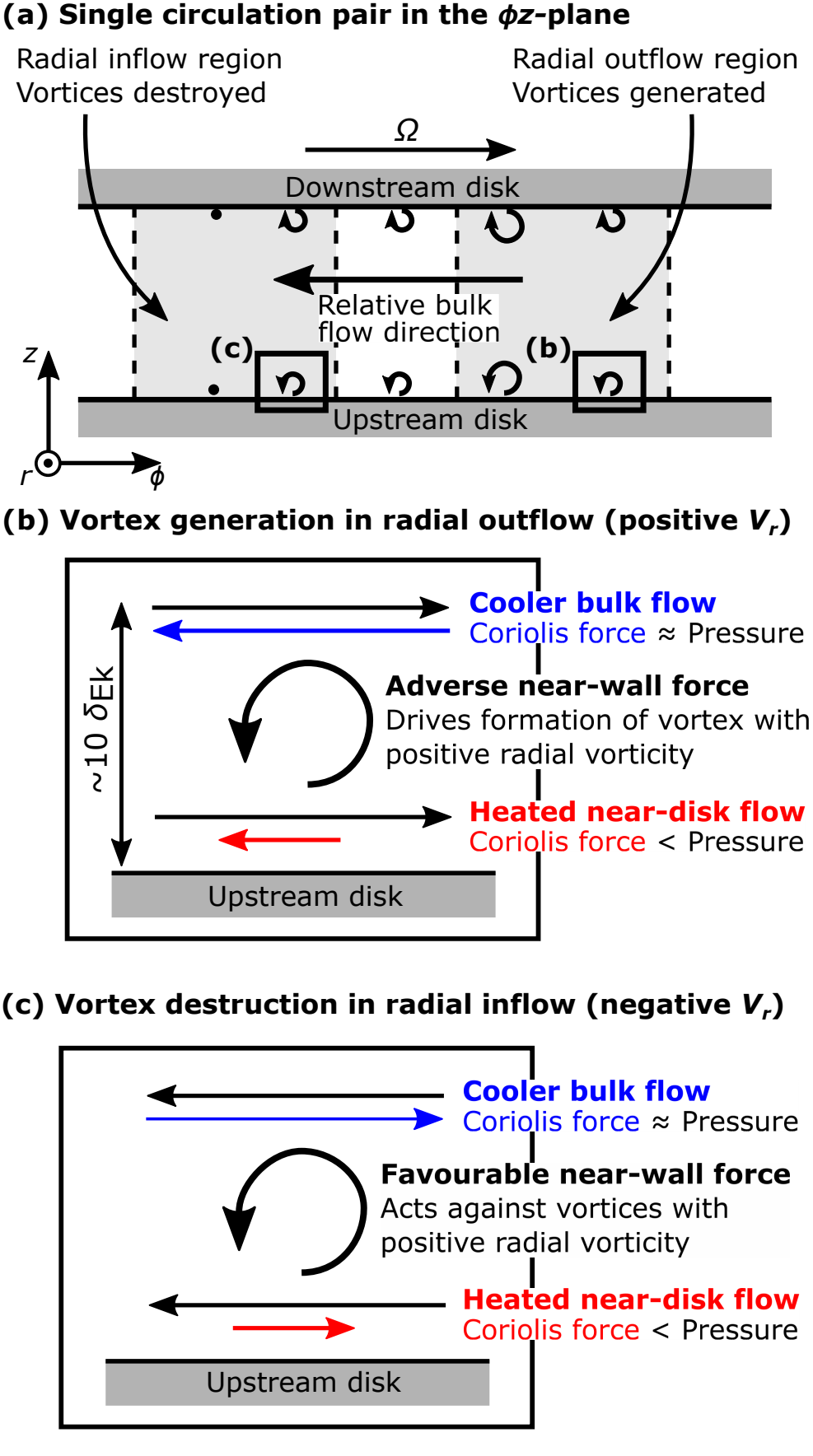

Fig. 19. ϕz-plane view of the mechanism for the formation of heating induced vortical instabilities in the anti-cyclonic circulation.

7 Conclusion

There is a strong incentive to consider CHT computations of rotating cavities due to the inherently conjugate nature of these flows. However, the application of CHT is challenging due to the need to use LES to capture the cavity aerodynamics - the characteristic time-scale of the solid-domain is greater than the small time-scales relevant in the fluid domain by a factor of 10,000, and simulating unsteady conduction introduces stringent mesh resolution requirements in the solid domain.

In this paper, we enable turbulence resolving CHT computations of rotating cavities by introducing a new multi-scale method for LES-CHT that extends previous work based on a local transfer function approach by He [11] to be able to capture low frequency unsteadiness directly in the solid domain through a time-spectral solution method. To illustrate ease of adoption in industrially relevant tooling, the new method is implemented, verified, and demonstrated in a commercial CFD solver.

The new methodology is applied to two different heating configurations of a cavity operating at the same bulk flow conditions as an experimental cavity studied by Bohn et al. [16]: a case heated axially via the disks (in a similar manner to the experimental cavity), and a cavity heated radially by conduction from the shroud (as would be the case in a gas turbine).

The formation of small-scale flow structures in key regions within the cavity is found to be strongly dependent on exactly how the cavity is heated, even for the same bulk flow description. The stronger shroud heating in the radially heated case causes buoyancy driven streaks to form, while in the axially heated case, vortical structures responsible for mixing hot near-disk and cold bulk flow were observed to form in radial outflow. To the authors' knowledge, this is the first time that the latter flow structure has been observed.

The heating induced flow structures in the near-disk flow are caused by the local reduction in density leading to a smaller stabilising local Coriolis in regions of radial outflow. It is notable that the effects of the vortical flow structures extend down to the disk, well below the laminar Ekman layer thickness. Their presence has implications for wider studies of rotating cavities: its effects are inconsistent with the laminar Ekman layer modelling argument commonly used when investigating rotating cavities, and it shows that disk heating may need to be taken into account when examining Ekman layer transition.

The fact that the same bulk description of the flow can have significantly different flow structures highlights the need to use high-fidelity thermal boundary conditions calculated from CHT when simu-

lating rotating cavities. This is necessary in order to properly capture the interplay of heating-dependent flow structures on the shroud and disk, and the solid domain conduction.

Acknowledgements

The authors would like to thank the UK Engineering and Physical Science Research Council (project reference 2117004) for supporting the first author's DPhil, and also to acknowledge the use of the University of Oxford Advanced Research Computing (ARC) facility[1] in carrying out this work.

[1] http://dx.doi.org/10.5281/zenodo.22558

Nomenclature

a	Cavity inner radius (m)
A_w, B_w	Wall temperature harmonics (K)
b	Cavity outer radius (m)
c	Specific heat capacity (J/kgK)
f	Frequency (Hz)
k	Thermal conductivity (W/mK)
Nu	Nusselt number
r, ϕ, z	Cylindrical coordinates (m, rad, m)
r_s	Shaft radius (m)
RMS	Root-mean-square
s	Shroud width (m)
T	Static temperature (K)
q	Heat flux (W/m^2)
V_r, V_z	Radial and axial velocities (m/s)
w	As a subscript - on the wall
W_ϕ	Relative tangential velocity (m/s)
δ_P	Thermal penetration depth (m)
δ_{Ek}	Laminar Ekman layer thickness (m)
ρ	Density (kg/m^3)
Ω	Rotational speed (rad/s)

References

[1] Hickling, T., and He, L., 2021. "Some observations on the computational sensitivity of rotating cavity flows". *Journal of Engineering for Gas Turbines and Power,* ***143***, 1.

[2] Saini, D., and Sandberg, R. D., 2021. "Large-eddy simulations of high rossby number flow in the high-pressure compressor inter-disk cavity". *Journal of Turbomachinery,* ***143***, 11.

[3] Puttock-Brown, M. R., Rose, M. G., and Long, C. A., 2017. "Experimental and computational investigation of rayleigh-bénard flow in the rotating cavities of a core compressor". pp. GT2017–64884.

[4] Puttock-Brown, M. R., and Rose, M. G., 2018. "Formation and evolution of rayleigh-bénard streaks in rotating cavities". pp. GT2018–75497.

[5] Gao, F., Pitz, D. B., and Chew, J. W., 2020. "Numerical investigation of buoyancy-induced flow in a sealed rapidly rotating disc cavity". *International Journal of Heat and Mass Transfer,* ***147***, p. 118860.

[6] Gao, F., and Chew, J. W., 2021. "Ekman layer scrubbing and shroud heat transfer in centrifugal buoyancy-driven convection". *Journal of Engineering for Gas Turbines and Power,* ***143***, 7.

[7] Sun, Z., Amirante, D., Chew, J., and Hills, N. J., 2015. "Coupled aerothermal modeling of a rotating cavity with radial inflow". *Journal of Engineering for Gas Turbines and Power,* ***138***, p. 032505.

[8] Amirante, D., Adami, P., and Hills, N. J., 2021. "A multifidelity aero-thermal design approach for secondary air systems". *Journal of Engineering for Gas Turbines and Power,* ***143***, 3.

[9] Tian, S., and Zhu, Y., 2012. "Disk heat transfer analysis in a heated rotating cavity with an axial throughflow". pp. GT2012–69185.

[10] He, L., and Oldfield, M. L. G., 2011. "Unsteady conjugate heat transfer modeling". *Journal of Turbomachinery,* ***133***, p. 031022.

[11] He, L., 2019. "Closely coupled fluid-solid interface method with moving-average for les based conjugate heat transfer solution". *International Journal of Heat and Fluid Flow,* ***79***, p. 108440.

[12] Incropera, F., Bergman, T., DeWitt, D., and Lavine, A., 2013. *Fundamentals of Heat and Mass Transfer*, 7 ed. Wiley.

[13] Fadl, M., and He, L., 2017. "On large eddy simulation based conjugate heat transfer procedure for transient natural convection". *Journal of Turbomachinery,* ***139***.

[14] Shahi, M., Kok, J. B., Casado, J. C. R., and Pozarlik, A. K., 2015. "Transient heat transfer between a turbulent lean partially premixed flame in limit cycle oscillation and the walls of a can type combustor". *Applied Thermal Engineering,* ***81***, 4, pp. 128–139.

[15] He, L., 2013. "Fourier spectral modelling for multi-scale aero-thermal analysis". *International Journal of Computational Fluid Dynamics,* ***27***, pp. 118–129.

[16] Bohn, D., Deutsch, G. N., Simon, B., and Burkhardt, C., 2000. "Flow visualisation in a rotating cavity with axial throughflow". pp. 2000–GT–0280.

[17] He, L., 2021. "Averaging for high fidelity modeling-toward large eddy simulations in multi-passage multi-row configurations". *Journal of Turbomachinery,* ***143***, 2.

[18] Onori, M., Amirante, D., Hills, N. J., and Chew, J. W., 2016. "LES validation for a rotating cylindrical cavity with radial inflow". pp. GT2016–56393.

[19] Sagaut, P., 2006. *Large Eddy Simulation for Incompressible Flows*. Springer-Verlag.

[20] Mehdizadeh, O. Z., Vilmin, S., Tartinville, B., and Hirsch, C., 2017. "Nonlinear harmonic method applied to turbine conjugate heat transfer analysis for efficient simulation of hot streak clocking and unsteady heat transfer". pp. GT2017–63622.

[21] Long, C. A., 1994. "Disk heat transfer in a rotating cavity with an axial throughflow of cooling air". *International Journal of Heat and Fluid Flow,* ***15***, pp. 307–316.

[22] Owen, J. M., and Powell, J., 2006. "Buoyancy-induced flow in a heated rotating cavity". *Journal of Engineering for Gas Turbines and Power,* ***128***, 1, pp. 128–134.

[23] Özgen, S., 2004. "Effect of heat transfer on stability and transition characteristics of boundary-layers". *International Journal of Heat and Mass Transfer,* ***47***, 10, pp. 4697–4712.

[24] Schäfer, P., Severin, J., and Herwig, H., 1995. "The effect of heat transfer on the stability of laminar boundary layers". *International Journal of Heat and Mass Transfer,* ***38***, 7, pp. 1855–1863.